Introduction

Microseismic monitoring analyzes signals induced by hydraulic fracturing and is a powerful technique for assessing reservoir properties. Despite the absence of controlled sources, one can adapt methods from active seismic exploration to estimate microseismic event locations (Grechka and Heigl, 2017). Conventionally, Kirchhoff approaches (Kao and Shan, 2004) for microseismic imaging require significant traveltime picking, commonly ineffective for low signal-to-noise ratio microseismicity, and strong wave propagation assumptions (e.g., neglecting multipathing). Alternatively, wavefield imaging (Witten and Shragge, 2015) obviates traveltime picking and handles wave propagation in realistic models.

Wavefield imaging adapted to microseismic applications is usually implemented in two steps: (1) back-propagating data into an earth model; and (2) applying an imaging condition to extract the source location from the extrapolated wavefield. Generally, the imaging condition autocorrelates the 4D wavefield at zero-lag, generating a 3D image. Assuming correct velocities and proper treatment of source radiation patterns, the peak amplitude of the image suggests the true source location; however, not satisfying these assumptions can lead to significant event mislocation. For velocity improvement, relying solely on zero-lag wavefield autocorrelation is insufficient; therefore, wavefield correlation beyond zero lag provides the information to improve the migration velocities within the adjoint-state framework (Witten and Shragge, 2017). For multicomponent elastic imaging, the distinct wave modes (P and S) coexistent at the source enable a PS imaging condition, which is based on wave-mode decomposition and subsequent crosscorrelation of the decomposed wavefields. However, for anisotropic earth models, wave-mode decomposition is required at each extrapolation time step, impeding a fast implementation. Also, the elastic PS correlation does not properly handle the different P- and S-polarizations, producing a nodal plane (i.e., a zero) at the estimated source location instead of an expected peak amplitude.

We aim to address such shortcomings of the multicomponent PS imaging condition that are detrimental to imaging and velocity inversion. By substituting PS correlation with energy correlation (Rocha et al., 2017), we propose an imaging condition for passive seismic applications that produces a peak amplitude at the estimated source location, precludes wave-mode decomposition at each time step, and complements the PS imaging condition with improved focusing attributes for microseismic migration velocity analysis. We explain how such imaging condition is adapted to passive imaging scenarios, and demonstrate its effectiveness in locating microseismic sources using realistic 3D synthetic examples.

Theory

The anisotropic elastic wave equation may be written as

$$\rho\ddot{\mathbf{U}} = \nabla\cdot\left(\underline{\underline{\mathbf{c}}}\nabla\mathbf{U}\right)\ , \tag{1}$$

where $\mathbf{U}(\mathbf{x},t)$ represents a space-time displacement field, $\rho(\mathbf{x})$ is the medium density, $\underline{\underline{\mathbf{c}}}(\mathbf{x})$ is the stiffness tensor, and superscript dots indicate time derivative. Assuming isotropy, equation 1 reduces to

$$\ddot{\mathbf{U}} = V_P^2\nabla(\nabla\cdot\mathbf{U}) - V_S^2\nabla\times(\nabla\times\mathbf{U})\ , \tag{2}$$

where $V_P(\mathbf{x})$ and $V_S(\mathbf{x})$ are the P- and S-wave velocities, respectively. Using multicomponent data recorded at the receivers, $\mathbf{U}$ can be extrapolated throughout either an anisotropic (equation 1) or isotropic (equation 2) earth model. Without loss of generality, we assume isotropy in our numerical experiments to handle only a single shear-wave mode for simplification.

Commonly, elastic imaging conditions decomposes $\mathbf{U}$ into its P- and S-wave mode constituents using Helmholtz decomposition (Dellinger and Etgen, 1990):

$$P = \nabla\cdot\mathbf{U}\ ,\ \ \mathbf{S} = \nabla\times\mathbf{U}\ , \tag{3}$$

where $P(\mathbf{x},t)$ is a scalar wavefield containing the compressional wave mode, and $\mathbf{S}(\mathbf{x},t)$ is a vector wavefield containing the transverse wave mode; equation 3 is valid only for isotropic media. Separated wave modes by equation 3 enable a cross-correlation PS imaging condition (Artman et al., 2010):

$$I_{PS}(\mathbf{x}) = \sum_t P\|\mathbf{S}\|\ , \tag{4}$$

which produces a nodal plane, whose opposite polarity side lobes indicate the source position at the zero crossing. In contrast, Rocha et al. (2017) define an imaging condition applicable to arbitrary anisotropy:

$$I_E(\mathbf{x}) = \sum_t \left[\rho \dot{\mathbf{U}} \cdot \dot{\mathbf{U}} - \left(\underline{\underline{\mathbf{c}}} \nabla \mathbf{U} \right) : \nabla \mathbf{U} \right], \tag{5}$$

which attenuates events within $\mathbf{U}$ sharing the same polarization and propagation directions. Such events hamper image quality with spurious artifacts. Meanwhile, at the source, the correlation between P- and S-wave modes is preserved, producing a peak amplitude instead of a nodal plane as in the PS correlation.

Although based on zero-lag correlation, both imaging conditions are actually special cases of a more general wavefield comparison. Extending wavefield correlation beyond zero lag enables velocity improvement using extended images (Witten and Shragge, 2015), which for equation 4 correspond to

$$I_{PS}(\mathbf{x}, \boldsymbol{\lambda}) = \sum_t P(\mathbf{x} + \boldsymbol{\lambda}, t) \, \| \mathbf{S}(\mathbf{x} - \boldsymbol{\lambda}, t) \| , \tag{6}$$

where $\boldsymbol{\lambda}$ is the spatial lag. For the imaging condition in equation 5, we adopt a similar approach to write

$$I_E(\mathbf{x}, \boldsymbol{\lambda}) = \sum_t \left[\rho(\mathbf{x} + \boldsymbol{\lambda}) \dot{\mathbf{U}}(\mathbf{x} + \boldsymbol{\lambda}, t) \cdot \dot{\mathbf{U}}(\mathbf{x} - \boldsymbol{\lambda}, t) - \underline{\underline{\mathbf{c}}}(\mathbf{x} + \boldsymbol{\lambda}) \nabla \mathbf{U}(\mathbf{x} + \boldsymbol{\lambda}, t) : \nabla \mathbf{U}(\mathbf{x} - \boldsymbol{\lambda}, t) \right] . \tag{7}$$

In general, one can estimate velocity accuracy on extended images by evaluating how focused the events are around zero space lag. Besides evaluating image quality with correct velocities, we investigate the extended PS and energy images to infer potential applications on velocity estimation.

Examples

First, we investigate the velocity sensitivity of both imaging conditions. We model a forward-propagated wavefield using a stress source at the center of a cube, 16Hz Ricker wavelet, constant velocity ($[V_P, V_S] = [3.0, 1.8]$km/s), and record multicomponent data at surface receivers with sparse and fixed spacing ($\Delta x = \Delta y = 0.25$km). We then backpropagate the modeled data with correct and incorrect velocities (globally perturbed by $\pm 8\%$) and apply the discussed imaging conditions. For incorrect velocities, although the correlation between P- and S-waves would occur at a different location from that of the true source, we would still expect a coherent pattern that would be useful for migration velocity analysis. Figures 1a-1c and 1d-1f show the zoomed 2D slices of the PS (I_{PS}) and energy (I_E) image volumes, respectively. Note how the imaged events exhibit misfocusing when using incorrect velocities, and that all PS images have a zero crossing at the point of maximum correlation (e.g., at $x = y = z = 2$km in Figure 1b). However, for I_E computed with incorrect velocities (Figure 1d and 1f), we observe a more straightforward and interpretable moveout pattern from the misfocused events relative to I_{PS}, as well as an absence of visible nodal planes. At the correct velocity, I_E (Figure 1e) exhibits a focused correlation (with peak amplitude) at the source location as opposed to I_{PS} in Figure 1b.

Our second numerical test compares the imaging conditions using the more complex SEG/EAGE 3D overthrust model (Aminzadeh et al., 1994). We use a source at the center of a model subset ($x = y = 3.048$km, $z = 1.073$km), and a realistic distribution of 192 multicomponent receivers (Figure 2b). Since the original model contains only V_P, we arbitrarily create V_S using a variable V_P/V_S as a function of depth. Then, we model (with a stress source) and backpropagate the recorded data, and compute I_E and I_{PS}. Figures 2c and 2d show I_{PS} and I_E zoomed around the source location, respectively. The image locations colored in red represent clipped amplitudes. I_{PS} (Figure 2c) positions the clipped amplitudes about 200m away from the source location, mainly due to the zero crossing at the known source location. However, I_E (Figure 2d) has the clipped amplitudes within one grid cell of the true source location. Therefore, the images in Figures 2c and 2d emphasize the more consistent focusing of I_E relative to I_{PS}, and the misplacement of the clipped peak amplitude for I_{PS}. Also, we generate extended images for both I_E and I_{PS} using the correct velocity only (Figures 2e and 2f). As expected, $I_{PS}(\mathbf{x}, \boldsymbol{\lambda})$ has a nodal plane at zero lag and exhibits substantial unfocusing away from zero lag even though the velocities are exact. $I_E(\mathbf{x}, \boldsymbol{\lambda})$ shows a more focused event at zero lag without nodal planes.

Conclusions

For passive wavefield imaging with surface-recorded multicomponent data, the energy imaging condition offers an improved solution for locating seismic sources with an arbitrary earth model. We demon-

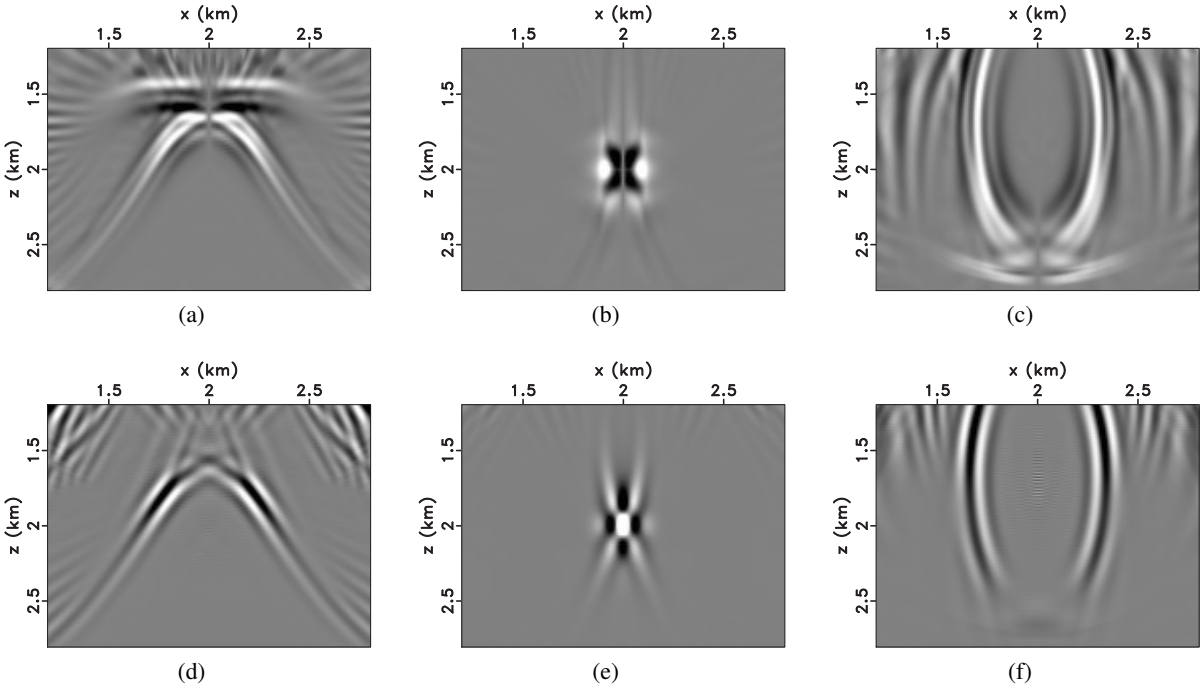

Figure 1: I_{PS} and I_E with (a/d) $[+8\%V_P, -8\%V_S]$ and (c/f) $[-8\%V_P, +8\%V_S]$ perturbations; and (b/e) correct velocities, respectively. Note the misfocused events with respect to the focused correlation in the central panels (which use the correct velocity), and how I_E exhibits fewer side lobes (d and f) and a peak amplitude at the source location for the correct velocity (e), as opposed to I_{PS}.

strate that I_E exhibits better attributes than I_{PS} in terms of image quality and velocity sensitivity, since it produces a peak amplitude at the source location with fewer imaging artifacts. The improved imaging attributes are also present in the extended domain, suggesting its application for microseismic velocity analysis. The absence of wave-mode decomposition in our method permits incorporating anisotropy without significant additional computational cost, as opposed to the conventional PS imaging condition that relies on expensive wave-mode decomposition for anisotropic media.

Acknowledgements

We thank the sponsors of the Center for Wave Phenomena for their support of this research. Our reproducible numeric examples use the Madagascar open-source software freely available at www.ahay.org.

References

Aminzadeh, F., Burkhard, N., Nicoletis, L., Rocca, F. and Wyatt, K. [1994] SEG/EAEG 3-D modeling project: 2nd update. *The Leading Edge*, **13**(9), 949–952.

Artman, B., Podladtchikov, I. and Witten, B. [2010] Source location using time-reverse imaging. *Geophysical Prospecting*, **58**(1), 861–873.

Dellinger, J. and Etgen, J. [1990] Wave-field separation in two-dimensional anisotropic media. *Geophysics*, **55**(7), 914–919.

Grechka, V. and Heigl, W. [2017] *Microseismic Monitoring*. Society of Exploration Geophysicists.

Kao, H. and Shan, S. [2004] The source-scanning algorithm: Mapping the distribution of seismic sources in time and space. *Geophysical Journal International*, **157**, 589–594.

Rocha, D., Tanushev, N. and Sava, P. [2017] Anisotropic elastic wavefield imaging using the energy norm. *Geophysics*, **82**, S225–S234.

Witten, B. and Shragge, J. [2015] Extended wave-equation imaging conditions for passive seismic data. *Geophysics*, **80**(6), WC61–WC72.

Witten, B. and Shragge, J. [2017] Image-domain velocity inversion and event location for microseismic monitoring. *Geophysics*, **82**(5), KS71–KS83.

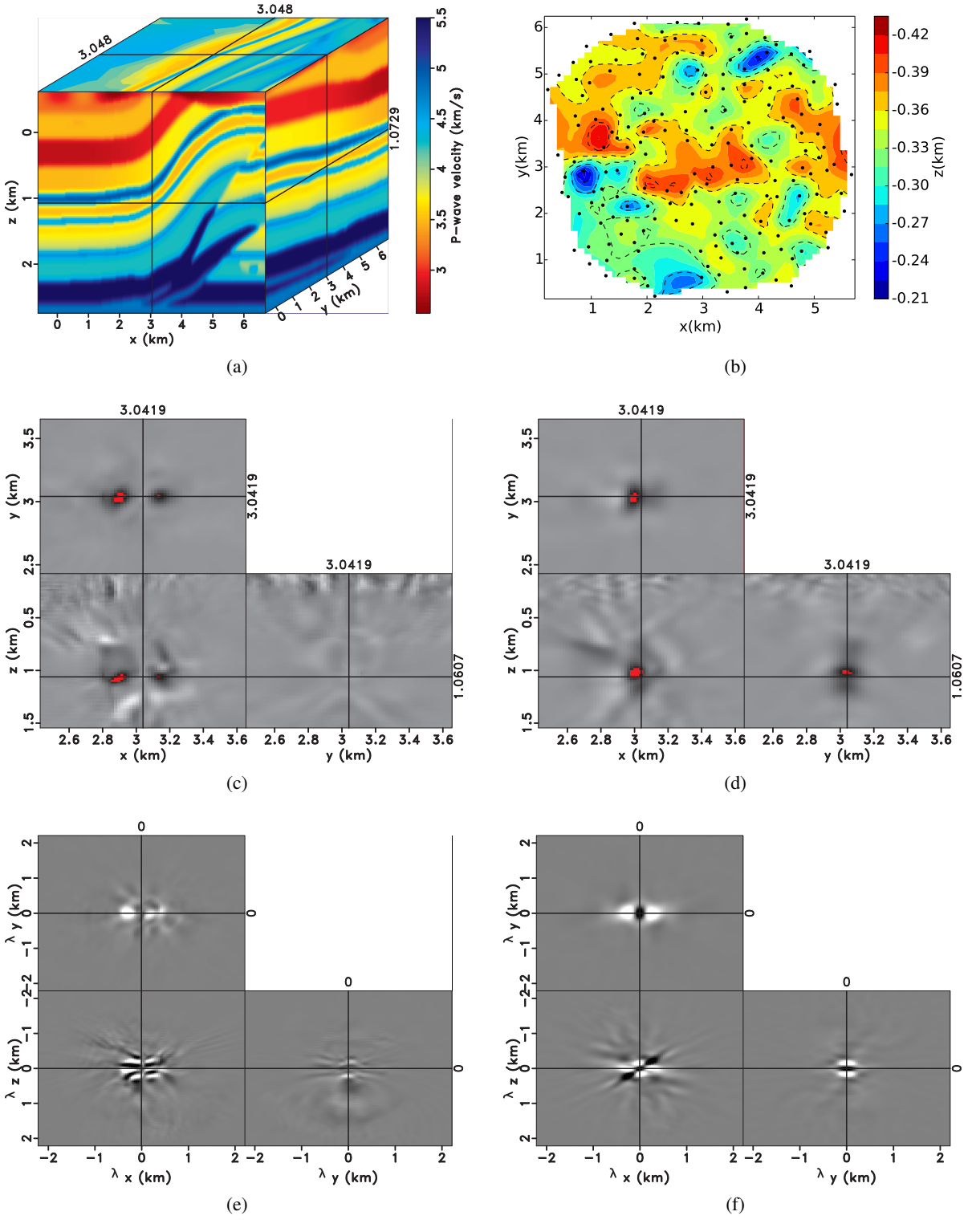

Figure 2: SEG/EAGE overthrust experiment: (a) P-wave velocity model. (b) Receiver coordinates with realistic areal distribution and elevation. Zoomed (c) $I_{PS}(\mathbf{x})$ and (d) $I_E(\mathbf{x})$, as well as (e) $I_{PS}(\mathbf{x},\boldsymbol{\lambda})$ and (f) $I_E(\mathbf{x},\boldsymbol{\lambda})$. I_E positions peak amplitudes (in red) closer to the source location in (d) when compared to (c), and a more focused event in the extended domain in (f) when compared to (e).